Nanoscale

PAPER

View Article Online
View Journal | View Issue

Cite this: *Nanoscale*, 2021, **13**, 2693

Nonlinear detour phase holography†

Bingxia Wang,[a] Xuanmiao Hong,[a] Kai Wang,*[a] Xin Chen,[b] Shan Liu,[c] Wieslaw Krolikowski,[c,d] Peixiang Lu*[a,e,f] and Yan Sheng*[c]

Received 2nd October 2020,
Accepted 4th January 2021

DOI: 10.1039/d0nr07069f

rsc.li/nanoscale

Nonlinear photonic crystals are capable of highly efficient nonlinear wavefront manipulation, providing a promising platform for compact and large-scale integrated nonlinear devices. However, the current nonlinear encoding methods for nonlinear photonic crystals inherently require a number of disordered and complex microstructures, which are quite challenging in a real fabrication process. Herein we propose and experimentally demonstrate a nonlinear detour phase method for nonlinear wavefront manipulation in nonlinear photonic crystals. With the proposed method, the designed nonlinear detour phase hologram only requires a set of basic building blocks with simple shapes, which are easy to fabricate by using the femtosecond laser writing technique. The second-harmonic hologram is demonstrated by designing the nonlinear detour phase patterns, and the quasi-phase-matching scheme in the second-harmonic holographic imaging process is also discussed. This study conceptually extends the conventional detour phase method into the nonlinear regime, offering new possibilities for compact nonlinear micro-devices with multi-functions.

Introduction

Nonlinear photonic crystals (NPCs), which are characterized by a spatially modulated second-order nonlinear coefficient ($\chi^{(2)}$),[1–5] are indispensable in nonlinear optical research and applications requiring optical frequency conversion. The modulated $\chi^{(2)}$ microstructure offers a set of reciprocal lattice vectors (RLVs) to compensate for the phase mismatch between the interacting waves in optical frequency conversion processes such that the energy exchange between these waves can occur efficiently, which is known as quasi-phase-matching (QPM).[6,7] Recently, many studies have reported on the nonlinear properties of NPCs, such as second-harmonic generation (SHG),[8–10] and sum- or/and difference-frequency mixing and spontaneous parametric down conversion (SPDC).[11–13] For example, the SHG conversion efficiency in NPCs may easily reach tens of percents.[14] Therefore, they show promising applications in highly efficient frequency conversion micro-devices,[15,16] implementation of entanglement sources, and integrated optical devices.[17–21]

More importantly, the reversal of the sign of $\chi^{(2)}$ can introduce an additional π-phase shift in the emitted nonlinear polarization wave. Therefore, the transverse patterning of $\chi^{(2)}$ inverted areas provides an efficient way of controlling the wavefront of the generated nonlinear wave.[22–25] As a comparison, nonlinear metasurfaces, which are also considered as candidates for nonlinear wavefront manipulation, show great potential in many novel nonlinear functionalities, such as beam steering, optical vortex, *meta*-lenses, and holographic imaging.[26–29] The $\chi^{(2)}$ modulation in NPCs is usually achieved with ferroelectric domain engineering in nonlinear optical crystals such as lithium niobate (LN),[30,31] lithium tantalate (LT),[32] strontium barium niobate (SBN),[33] and calcium barium niobate (CBN) crystals.[10,24] There are mainly two popular $\chi^{(2)}$ pattern encoding methods for NPCs: nonlinear computer-generated holograms (NCGHs) and nonlinear volume holography (NVH).[34,35] With both methods, second-harmonic (SH) wavefront shaping in NPCs has been experimentally conducted, leading to the demonstration of Hermite–Gaussian beams,[34,36] vortex beams,[8,37] Airy beams,[38] and other special beams[39,40] at a doubled frequency. In general, both NCGHs and NVH methods are universal and convenient for designing $\chi^{(2)}$ patterns. However, they show some limitations. First, as the theoretically calculated variation in $\chi^{(2)}$ is continuous from −1 to 1, its binary representation for the experimental fabrication

[a]*Wuhan National Laboratory for Optoelectronics and School of Physics, Huazhong University of Science and Technology, Wuhan 430074, China.*
E-mail: kale_wong@hust.edu.cn, lupeixiang@hust.edu.cn
[b]*School of Physics and Optoelectronics Engineering, Xidian University, Xi'an 710071, China*
[c]*Laser Physics Center, Research School of Physics, Australian National University, Canberra, ACT 2601, Australia. E-mail: yan.sheng@anu.edu.au*
[d]*Science Program, Texas A&M University at Qatar, Doha 23874, Qatar*
[e]*Guangdong Intelligent Robotics Institute, Dongguan 523808, China*
[f]*CAS Center for Excellence in Ultra-intense Laser Science, Shanghai 201800, China*

†Electronic supplementary information (ESI) available: Detailed derivation of the nonlinear detour phase method; measurement of the mean diameter of randomly distributed ferroelectric domains; high-quality nonlinear holographic imaging of letter 'H'; and comparison of holographic images reconstructed by a nonlinear detour phase hologram and a nonlinear binary phase hologram. See DOI: 10.1039/d0nr07069f

process needs to be used. This, therefore, induces SHG phase distortion, which to some extent may impose additional errors in the generated SH wavefront. Second, these design methods do not take into account the actual fabrication accuracy, which may be far lower than the theoretical expectation. In fact, the nonlinearity modulation patterns encoded with these two holographic methods are always as complicated as the 'quick response (QR) codes', featuring narrow (with a size even below the optical diffraction limit) and oddly shaped ferroelectric domains. This can lead to a large structural deviation between the theoretically calculated patterns and the experimentally fabricated patterns.[35] Therefore, the fabrication of such disordered and complex domain structures remains a big challenge for the state-of-the-art domain engineering technologies, such as traditional electric field poling or the latest femtosecond laser direct writing techniques.[30,31] Although in recent years, femtosecond laser direct writing, *i.e.* femtosecond laser poling and erasing techniques, have made significant progress in achieving finer pattern fabrication,[4,5,25,31] the current $\chi^{(2)}$ encoding methods are still not suitable for the existing fabrication technique. So far, the holographic imaging of complex patterns with these advanced laser direct writing techniques are still lacking.

In this study, we extend, for the first time, to our knowledge, the concept of a traditional detour phase method into the nonlinear optical regime to create nonlinear holograms for high-fidelity reconstruction of special optical beams. This proposed method to modulate a nonlinearity phase is of great potential in functional hologram design because it is very easy to implement in the fabrication processes and convenient to extend to three-dimensional (3D) NPCs. Specifically, the nonlinear detour phase holography utilizes a series of basic units to construct the whole hologram. In each basic unit, there exists the same number of antiparallel domains, arranged differently to generate specific phases in the holographic imaging process. Therefore, it avoids the appearance of complex 'QR code' patterns, achieving a more accurate and convenient fabrication process based on the current ferroelectric domain engineering techniques. Considering the superiority of ferroelectric domain engineering with infrared light over the traditional electric field poling, we employ the direct femtosecond laser induced ferroelectric domain inversion to fabricate nonlinear detour phase holograms in an as-grown ferroelectric $Sr_{0.75}Ba_{0.25}Nb_2O_6$ (SBN-75) crystal. An H-shaped SH holographic image in the far field is demonstrated, which is in good agreement with the theoretical designs. Moreover, the QPM scheme in the SH holographic imaging process is also discussed. This high-quality nonlinear wavefront shaping device on the NPC platform can pave the way for applications in nonlinear integrated photonics.

Theory of the nonlinear detour phase method

The nonlinear detour phase method is proposed to modulate the nonlinearity phase so that the wavefront of the holographic generation of a new frequency light can be manipulated. In this study, the simplest process of SHG is taken as an example to describe the principles of this method. The reconstruction of the target far-field SHG image is realized by properly locating a set of basic units consisting of antiparallel domains. The one-dimensional (1D) nonlinear detour-phase hologram can be regarded as a binary $\chi^{(2)}$ nonlinear diffraction grating, where the distance between the adjacent inverted domains determines the SHG phase gradient at this location, leading to different diffraction angles. The two-dimensional (2D) nonlinear detour phase hologram is more complex, but it offers more freedom and enables 2D wavefront shaping. Therefore, we present a detailed theoretical derivation of the 2D nonlinear detour phase method in the remainder of this section.

We are committed to reconstructing an arbitrary target SH complex amplitude distribution $u(x, y)$ in the far field with the nonlinear detour phase method. Here, we use a deductive approach showing how to use this method to create a particular nonlinear detour phase hologram for achieving the target SH field distribution. The nonlinear detour phase hologram is composed of a set of basic units, which are encoded for arbitrary control over the phases of the SH beam. Unlike in its linear counterpart,[41,42] the basic units are selected to be $\pm\chi^{(2)}$ microstructures. The basic units have the same number of antiparallel ferroelectric domains, but the arrangement of these domains is different for each unit. In order to describe the selection rule of these basic units, we need to define some parameters. As shown in Fig. 1a, the coordinates of the (n, m)-th basic unit can be written as $(n\delta_\nu, m\delta_\nu)$, where δ_ν is the side length of square basic unit (marked by the black square in the figure). Without loss of generality, we consider the width and height of the inverted domains (with $+\chi^{(2)}$) as $c\delta_\nu$ and $W_{nm}\delta_\nu$, respectively, and the surrounding area is filled with the $-\chi^{(2)}$ medium as background. The inverted domain is displaced from the center of the basic unit $(n\delta_\nu, m\delta_\nu)$ by $P_{nm}\delta_\nu$. We illuminate the $\chi^{(2)}$ hologram with a normally incident monochromatic plane wave with a uniform amplitude. A schematic illustration of the frequency conversion and holographic imaging process is shown in Fig. 1b. For the SHG process, the second harmonics emitted from the positive and negative $\chi^{(2)}$ areas have the same amplitude but a phase difference of π, which imposes a binary phase distribution to the generated SH light. Therefore, the total SH electric field, $h(\nu_x, \nu_y)$, considered as the superposition of the SH electric fields originating from each basic unit, can be written as follows:

$$h(\nu_x, \nu_y) = \sum_{n,m} h_{nm}(\nu_{xnm}, \nu_{ynm}) = \sum_{n,m} h_0 \cdot \exp\left(\pi i \cdot \mathrm{rect}\left(\frac{\nu_{xnm} - P_{nm}\delta_\nu}{c \cdot \delta_\nu}\right) \mathrm{rect}\left(\frac{\nu_{ynm}}{W_{nm} \cdot \delta_\nu}\right)\right), \quad (1)$$

where $\nu_{xnm} = \nu_x - n\delta_\nu$; $\nu_{ynm} = \nu_y - m\delta_\nu$; (ν_{xnm}, ν_{ynm}) is the coordinate in the basic unit coordinate system; h_0 is the constant amplitude; the products of the rect functions account for the finite dimension of the inverted domains. The Fourier trans-

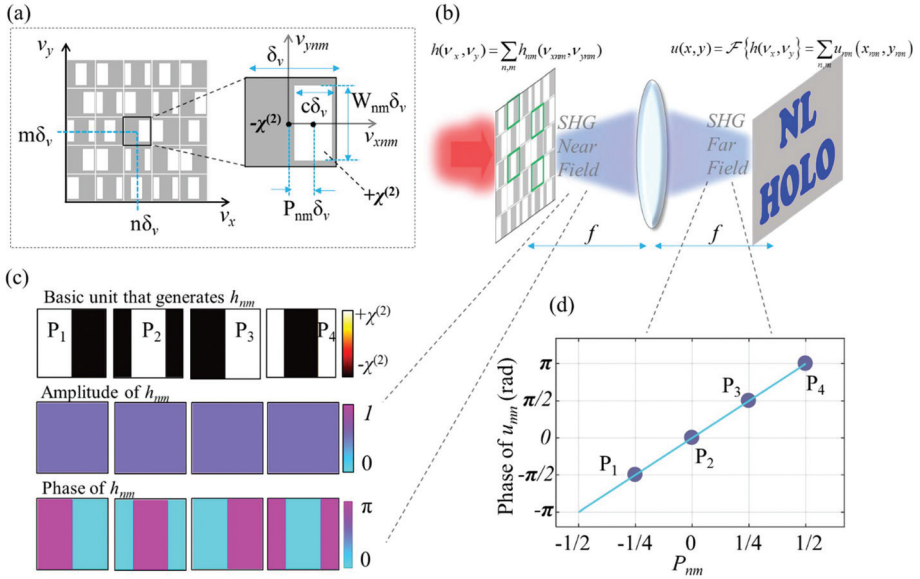

Fig. 1 General concept of the nonlinear detour phase method for frequency conversion and holographic imaging. (a) (left) Nonlinear detour phase hologram composed of a series of basic units; (right) structure of the (n, m)-th sampling basic unit, which is composed of antiparallel ferroelectric domains: the inverted positive (white) and negative (gray) domains showing opposite signs of the second-order nonlinearity $\chi^{(2)}$. The inverted domain is displaced from the center of the unit by $P_{nm}\delta_\nu$. (b) Schematic illustration of frequency conversion and holographic imaging caused by a plane wave at normal incidence and transmittance through the nonlinear hologram. The SHG electric field at near-field, $h(\nu_x, \nu_y)$ is composed of superposition of the transmitted electric field $h_{nm}(\nu_{xnm}, \nu_{ynm})$ from each basic unit; SHG electric field at the far field, $u(x, y)$, composed of superposition of the electric field $u_{nm}(x_{nm}, y_{nm})$ contributes to the target nonlinear holographic imaging. (c) Numerical demonstration of the nonlinear properties of the four basic units (P_1, P_2, P_3, P_4). (up) The structures of the four basic units; (middle and bottom) numerically simulated amplitude and phase of SHG after being transmitted through the corresponding units. (d) SHG phase shift after being transmitted through P_1, P_2, P_3, and P_4 units as a function of P_{nm}.

form of $h(\nu_x, \nu_y)$, which represents the complex electric field in the far field, is written as $u(x,y)$.

The desired SHG field at far field can also be expressed in a general form as follows:

$$u'(x,y) = \sum_{nm} A'_{nm} \exp(i\varphi_{nm}). \quad (2)$$

Equating the phase terms in expressions $u(x,y)$ and $u'(x,y)$ leads to a simple equation:

$$P_{nm} = \frac{\varphi_{nm}}{2\pi}, \quad (3)$$

where φ_{nm} is the phase shift of the transmitted SH in the far field generated by the (n, m)-th basic unit. The detailed derivation process is discussed in ESI Section 1.† Eqn (3) has the same form as that of its counterpart in the linear regime.[41,42] It shows that the SHG phase shift (φ_{nm}) from the (n, m)-th basic unit is determined by the distance between the center of the inverted domain and the center of the basic unit (P_{nm}). Since we set the width of the inverted domain to be half the width of the basic unit, when the inverted domain horizontally moves inside the basic unit from $-\delta_\nu/4$ to $\delta_\nu/4$, the induced detour phase varies from $-\pi/2$ to $\pi/2$. If the inverted domain overflows the basic unit, we apply overflow correction by moving the overflowing part to the other side of the unit, as in its linear counterpart,[41,42] to obtain the detour phase varying from $-\pi$ to $-\pi/2$ and $\pi/2$ to π. Therefore, the phase shift of SHG varies from $-\pi$ to π when the inverted up domain continuously shifts from the unit center from $-\delta_\nu/2$ to $\delta_\nu/2$. In order to avoid the appearance of very thin domains, we set the smallest width of the overflowing domain considering the practical fabrication accuracy, which is 1 μm in our case. To simplify the encoding process, we divide the continuous phase shift φ_{nm} into a number of discrete values. For instance, in this study, four discrete phases are used: $-\pi/2$, 0, $\pi/2$, and π, and the corresponding distances between the inverted domain and the center of the basic unit are $-\delta_\nu/4$, 0, $\delta_\nu/4$, and $\delta_\nu/2$, respectively. The widths of the smallest antiparallel domain and basic unit are 1 μm and 4 μm, respectively. The structures of the generated four basic units (P_1, P_2, P_3, P_4) with P_{nm} values of $-1/4$, 0, 1/4, and 1/2, respectively, are shown in Fig. 1c, where P_4 corresponds to the case of the inverted domain overflowing the basic unit. Fig. 1c also shows the numerically simulated homogeneous amplitude and binary phase of the emitted SHG after passing through the four basic units (the middle and bottom rows in the figure). According to the theorem of Fourier optics, after transmitting through P_1, P_2, P_3, and P_4 units, the SHG phase shifts at the far field are $-\pi/2$, 0, $\pi/2$, and π, respectively. The SHG phase shift as a function of P_{nm} is shown in Fig. 1d.

The nonlinear detour phase holography is a practical and flexible method because one can divide the continuous phase

shift φ_{nm} into different number of discrete values, depending on the complexity of the target wavefront. In our case, four discrete phases are sufficient to generate an H-shaped SH field, while for a more complex target wavefront, eight discrete phase values may be required and the width of each basic unit will be doubled.

Hologram design

In this section, we use the above mentioned nonlinear detour phase method to design a practical example of a hologram to realize an H-shaped SH image based on the four basic units (P_1, P_2, P_3, P_4). Here, we define the hologram plane as the far-field plane shown in Fig. 1b, and the object plane as the image plane of the target H-shaped SHG. The electric fields in both planes are directly connected to each other by a Fourier transform. At first, we calculate the corresponding SHG phase distribution at the hologram plane from the target H-shaped SHG intensity pattern at the object plane using the iterative Fourier transform algorithm (IFTA).[43] The electric field at the object plane consists of an H-shaped amplitude and a random phase as the initial input; in the process of multiple iterations, we fix the amplitudes at the object plane as H-shape and those at the hologram plane as an arbitrary constant; the corresponding phase distribution at the hologram plane can be calculated if the Fourier transform of the electric field at the hologram plane yields the target H-shaped image. The obtained phase varies continuously from $-\pi$ to π, so we divide it into four discrete values: $-\pi/2$, 0, $\pi/2$, and π. In Fig. 2a, we schematically show the targeted H-shaped far-field SHG image and the corresponding phase map at the hologram plane. Then, the hologram can be constructed by encoding these four phase values with the four holographic units (P_1, P_2, P_3, P_4). Fig. 2b shows the calculated ferroelectric domain pattern with this nonlinear detour phase method. It also shows the selection of the four basic units (the marked four areas in the figure). Considering the practical fabrication accuracy of ferroelectric domain engineering, the sizes of the basic units are selected to be 4×4 μm^2. This gives rise to the narrowest inverted domain fabricated to be 1 μm.

In experiment, the as-grown z-cut SBN-75 crystal was used to fabricate the nonlinear detour phase hologram. Ferroelectric domain inversion was performed by using a direct femtosecond poling technique.[31] More details of the hologram fabrication are provided in the Methods section. The engineered nonlinear detour phase hologram consists of a series of stripe-shaped inverted domains, which are shown in white in Fig. 2b and green in Fig. 2c and d, respectively. The 3D visualization of the fabricated ferroelectric domain structure is obtained with Čerenkov SH microscopy,[44] and the result is shown in Fig. 2c. The size of this laser-written domain area is 152×152 μm^2 in the xy plane, and the thickness of the inverted domains along the z-axis is ~30 μm. An expanded 2D view of the domain layer at a fixed depth inside the crystal is shown in Fig. 2d, where the insets depict the enlarged domain structure corresponding to the four basic units in a size of 4×4 μm^2, which have a good match with the numerically designed domain patterns. The smallest width of the inverted domain is about 1 μm.

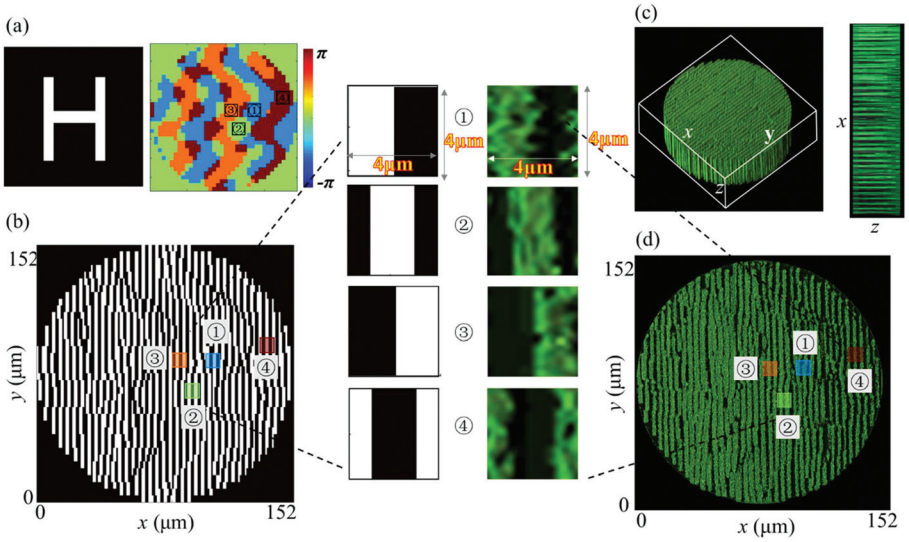

Fig. 2 Schematic diagrams illustrating the design and fabrication of the nonlinear detour phase hologram with all-optical ferroelectric domain engineering technique. (a) (left) The target SHG image in a form of letter 'H'; (right) SHG phase at the hologram plane calculated by IFTA and the phase values at the marked positions ①, ②, ③ and ④ are $-\pi/2$, 0, $\pi/2$, and π, respectively. (b) The calculated hologram obtained by placing the four basic units at the corresponding grids; the insets show the enlarged domain pattern at the marked four positions with a size of 4×4 μm^2. (c) The 3D visualization of the domain structure by Čerenkov SH microscopy.[44] (d) The fabricated ferroelectric domain structure in the xy plane, with the insets showing an expanded view of the domain structure for the four basic units.

Results and discussion

To verify the proposed nonlinear detour phase method, the SH holographic imaging from the designed hologram was experimentally studied. We perform a fixed wavelength measurement using the light source from a mode-locked Ti-sapphire femtosecond laser centered at 810 nm (Vitara Coherent, 8 fs and 80 MHz). The schematic representation of the experimental setup is shown in Fig. 3a. To tune the polarization state and average power of the incident beam, a half-wave plate (HW) and a polarizer (P) were used. The fundamental-frequency beam loosely focused by a lens L1 (f = 8 μm) pumped the hologram sample (S). After being spectrally filtered, the emitted SH signal was collected by lens L2 (f = 5 μm), and was fed into a CMOS camera (CCD) and a spectrometer. Lens L2 was mounted on a z-translation stage, which enabled the SHG intensity measurements either in the far field or the near field. Lens L3 (f = 10 μm) was only used in the near-field imaging process. More details of the SH signal measurement can be found in the Methods section.

The H-shaped SH beam in the far-field was observed under an excitation of a 200 mW pump laser, and the recorded image is shown in Fig. 3b (left). The corresponding 3D intensity profile is shown in Fig. 3b (right), for which a proper image processing involving denoising and high-resolution reconstruction was used for a better visualization effect. For comparison, we also conducted the numerical simulation of SH diffraction with the fabricated hologram, using the split-step fast Fourier transform based beam propagation method.[45] The numerically simulated far-field SHG intensity distribution and the optimized 3D intensity distribution are shown in Fig. 3c. A good agreement between the experimental and simulation results is clearly seen. The experimentally measured H-shaped beam shows more noise than the simulated one. A possible reason is that the ferroelectric domain structures used in the simulation were assumed to be constant along the propagation direction of the fundamental beam. However, in the real sample, the parameters of the ferroelectric domain structures, such as the width and length of the inverted domains, also slightly vary with the beam propagation. The randomly changed duty cycles and distances between the neighboring inverted domains will lead to a rather weak SHG as a background noise.

It should be noted that, during the design of the holographic phase plate, we used as few pixels as possible, *i.e.* 1124 pixels in total, to reduce fabrication difficulty and hologram size. This size-limited phase plate imposes a negative effect on the quality of the nonlinear holographic image. In order to achieve a high-quality holographic image with the proposed nonlinear detour phase method, it is necessary to increase the pixel number of the phase plate and the fabrication accuracy (for a limited hologram size). The detailed numerical simu-

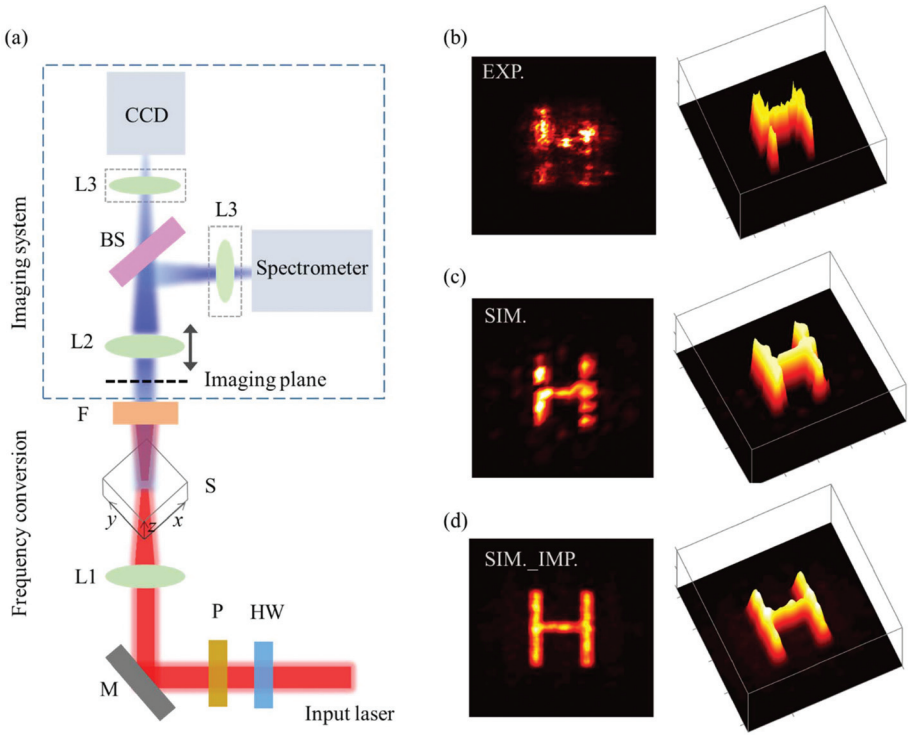

Fig. 3 Nonlinear holographic imaging with a fundamental wavelength of 810 nm. (a) The schematic sketch of the experimental setup. HW: half-wave plates; P: polarizer; M: mirror; L1: 10 cm lens; F: band-pass filter; L2: 5 cm lens; BS: beam splitter; L3: 10 cm lens (used only in the near-field imaging system). (b) Experimentally measured SHG holographic image in the far-field with a CMOS camera. (c) Numerically simulated far-field SHG intensity distribution. (d) The quality-improved simulation result using the phase plate with a pixel number of 18168.

lations of a quality-improved nonlinear holographic imaging of letter 'H' with pixel numbers of 4548 (with 1-μm fabrication resolution) and 18168 (with 0.5-μm fabrication resolution) are discussed in ESI Section 3.† The quality-improved simulation result using the phase plate with pixel number of 18168 is shown in Fig. 3d. It indicates that this proposed nonlinear detour phase method has the capability to achieve high quality image reproduction as long as the information capacity coded inside the hologram is large enough. In addition, a comparison of the holographic images of '*hot coffee*' reconstructed by the nonlinear binary phase hologram and the proposed nonlinear detour phase hologram (the pixel number of the phase plate and fabrication resolution setting are 7860 and 1 μm, respectively) is discussed in ESI Section 4.† ESI Fig. S3† shows that a nonlinear binary phase hologram is always accompanied by large processing errors leading to a low holographic imaging quality, while as a simple and efficient method, this proposed nonlinear detour phase hologram plays an important role in the improvement of image quality.

It is known that this efficient nonlinear frequency conversion process requires the fulfilment of phase matching conditions. By measuring and analyzing the emission angles of the SHG, we confirm that the frequency doubling process in our case was generated *via* nonlinear Raman–Nath diffraction.[46] We calculated the Fourier spectrum of the fabricated hologram, which exhibits a pair of H-shaped RLVs in the Fourier space, as shown in Fig. 4a. The magnitude of the RLVs corresponding to the center of the letter H was 1.57 μm^{-1}, which corresponds to the nonlinear Raman–Nath SH emission at an angle of ±5.74° (calculated with the refractive index from ref. 47) with respect to the propagation direction of the fundamental beam. The nonlinear Raman–Nath phase matching scheme refers to the situation wherein the transverse component of the QPM conditions is fulfilled, *i.e.*, $k_2 \cdot \sin(\theta) = G$ with G representing RLVs. The experimentally measured emission angle is ±(5.8° ± 0.5°), agreeing well with the calculated value. It should be noted that the SHGs from the nonlinear detour phase hologram are not collinear with the fundamental beam, but are distributed symmetrically on both sides of the fundamental beam. These two SH beams have the same spatial profile and symmetric emission angle. This character is useful for many applications such as the spatial manipulation of entangled photons *via* spontaneous parametric down conversion.[48]

In addition to demonstrating the nonlinear analogue of the detour hologram, we took the opportunity to use the hologram structure to demonstrate the self-imaging effect in the near-field, the so-called nonlinear Talbot effect.[49] Fig. 4b (left) shows the SH self-imaging, *i.e.*, the stripe-shaped domain pattern of the nonlinear hologram. Fig. 4b (right) shows the zoom-in of the nonlinear Talbot images of the marked area and the four typical building units (P_1, P_2, P_3, P_4). The measured dependence of the SH power on the pump power of the fundamental beam is shown in Fig. 4c. The quadratic fit (red curve) agrees well with the experimental data (black circles).

It should be noted that in the derivation of the mathematical principles of the nonlinear detour phase method, we used an ideal medium approximation, *i.e.*, we supposed that the nonlinear coefficient was positive ($+\chi^{(2)}$) in the laser poled

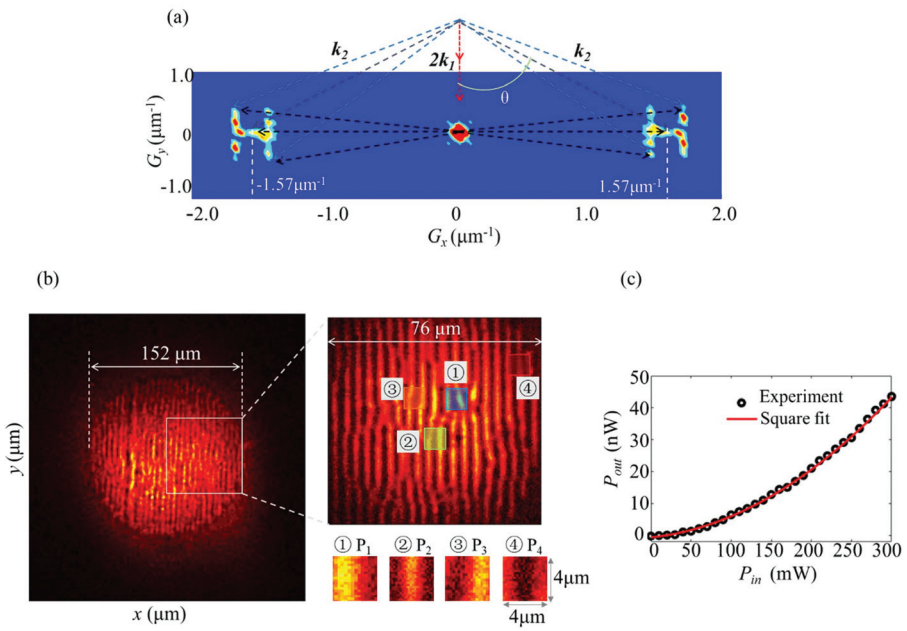

Fig. 4 Illustration of the nonlinear Raman–Nath-type QPM in the nonlinear detour hologram. (a) Fourier spectrum, *i.e.*, the distribution of reciprocal vectors calculated from the experimentally engineered hologram and the nonlinear Raman–Nath-type QPM scheme. (b) Hologram induced SH self-image at the first Talbot plane[49] (left) and the zoom-in nonlinear Talbot images of the marked area and the four typical building units (P_1, P_2, P_3, P_4) (right). (c) Dependence of the output SH power on the pump power at a fundamental wavelength of 810 nm.

areas and negative ($-\chi^{(2)}$) in the background area. However, the nonlinear detour phase hologram was fabricated in the as-grown SBN-75 crystal, which consisted of oppositely oriented and spatially randomly distributed submicron size ferroelectric domains.[50] The laser writing resulted in a uniform $+\chi^{(2)}$ in the processed areas representing the holographic pattern, leaving the randomly distributed antiparallel domains as a background. This disordered nonlinear background in the real hologram is equivalent to an optical medium with a nonlinear coefficient equal to zero (linear background).

To investigate the impact of the totally random ferroelectric domains surrounding the nonlinear holographic patterns, we numerically simulated SHG intensity distribution and its dependence on three kinds of backgrounds, *i.e.*, a uniform $-\chi^{(2)}$ background (left column), a random nonlinear background (middle column) and a linear background (right column). Fig. 5a shows the four basic units (P_1, P_2, P_3, P_4) with different backgrounds. The mean diameter of antiparallel domains in the random nonlinear background is selected as 100 nm, which was measured using an atomic force microscope (Bruker Dimension Edge) in the piezoelectric force microscope (PFM) mode (ESI Fig. S1†). Fig. 5b shows the nonlinear detour phase holograms with different backgrounds. Fig. 5c shows the corresponding Fourier spectrum, which exhibits a pair of H-shaped RLVs. With the split-step fast Fourier transform based beam propagation method,[45] we numerically simulated the far-field SHG intensity distribution when an input power fixed fundamental beam (centered at 810 nm) is incident on each of these three holograms. The well-controlled H-shape SH emissions are obtained in all these cases, as shown in Fig. 5d. However, it is clear that the background affects the intensity of the SHG. To quantitatively demonstrate the difference, we calculated the total integrated SHG intensity inside the green line marked area in Fig. 5d. It shows the equal SHG intensity emitted from the holograms with random nonlinear and linear backgrounds, which is one quarter of that from an ideal hologram with a uniform $-\chi^{(2)}$ background.

This behavior can be understood by considering the fact the random background does not contribute to the efficient emission of coherent SH signal in the geometry of interaction

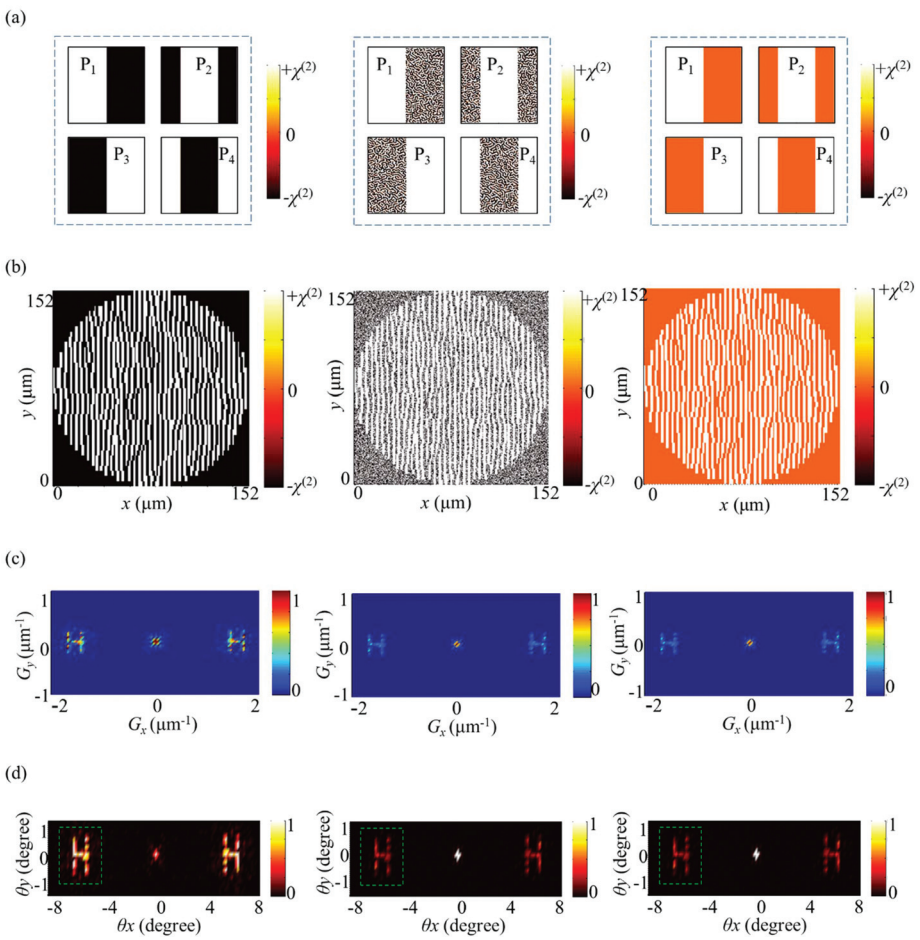

Fig. 5 SHG distribution generated from the designed nonlinear detour phase holograms with different backgrounds. (Left column) uniform $-\chi^{(2)}$ background; (middle column) random $\pm\chi^{(2)}$ nonlinear background; (right column) linear background. (a) The structures of the four basic units (P_1, P_2, P_3, P_4) with P_{nm} values of −1/4, 0, 1/4, and 1/2, respectively. (b) Constructed holograms with the four holographic units (P_1, P_2, P_3, P_4) for the nonlinear generation of an H-shaped image restoration. (c) The distribution of reciprocal lattice vectors calculated from the corresponding holograms. (d) Numerically simulated far-field SHG intensity distribution.

in this study,[51] *i.e.*, the fundamental beam propagating along the *z*-axis of the crystal, and hence does not affect the holographic imaging of the target object. As the effective nonlinear coefficient is zero in the random background regions (instead of $-\chi^{(2)}$ for the uniform crystal), the effective nonlinearity modulation is half of the original value, leading to four times lower SH signal as a result of the quadratic dependence of the SH intensity on the strength of nonlinearity.

It should be noted that the inverted nonlinear structure surrounded by a linear background is equivalent to a linear structure surrounded by a nonlinear background. The latter case is a typical structure fabricated by femtosecond laser erasing technique.[25] Therefore, this presented simulation of the first case (with a linear background) indicates that the proposed nonlinear detour phase method is also suitable for a sample fabricated by the femtosecond laser erasing technique. We believe that presenting the simulation of a linear background can inspire a wider interest in this nonlinear detour phase method.

Conclusion

In conclusion, we introduced the concept of nonlinear detour phase holography for generating coherent SH light with an arbitrary wavefront. The designed nonlinear detour phase hologram comprising basic units as building blocks can provide phase discontinuities across the surface; thus the emitted SH wavefront can be completely manipulated. The relationship between the SHG phase shift and the arrangements of antiparallel domains inside the basic unit is established theoretically. The simplified basic units not only ensure the fabrication accuracy, but also can be easily engineered by laser direct writing technology. Combining the proposed nonlinear detour phase holography and the advanced femtosecond laser domain inversion technique, we presented the first experimental demonstration of an H-shaped SH detour phase hologram, and then we discussed the QPM scheme in the nonlinear holographic imaging process. This study provides an alternative way to obtaining coherent light with predesigned shapes at new frequencies. We envision that this study not only can be easily extended to the 3D nonlinear holographic imaging of complex patterns, but also promises the integration of linear and nonlinear optoelectronic multiple functional devices due to the compatibility with other existing optical manufacturing techniques on NPC platforms.

Methods

Nonlinear detour phase hologram fabrication

A femtosecond writing optical beam from an oscillator (Coherent, Mira) operating at 800 nm was tightly focused by a 50× microscope objective (NA = 0.65), and the focus was located about 45 μm below the surface of the SBN-75 sample. The average poling power of the laser beam was 290 mW. The SBN-75 sample was mounted on a computer-controlled *xyz* translation stage. To implement ferroelectric domain inversion, first the shutter was opened for 0.1 s and then the crystal was translated against the incident beam along the *z*-axis with an average speed of 2.5 mm s^{-1}. After this process, the shutter was closed, and the beam moved to the next position to repeat the domain inversion process. Optical poling relies on a nonlinear absorption process of femtosecond laser pulses, and induces a thermoelectric field and consequently rearranges the ferroelectric domains along this field in the focal volume of the beam. Stripe-shaped inverted domains with different lengths were produced by keeping a small distance (0.5 μm) between the neighboring domain spots to make them merge.

Nonlinear holographic imaging measurement

A mode-locked Ti-sapphire femtosecond laser system (Vitara Coherent, 8 fs and 80 MHz) was used to provide the fundamental-frequency beam at 810 nm. The polarization state and average power of the fundamental beam were controlled by the combination of a half-wave plate (HW) and a polarizer (P). Then, a lens L1 (focal length f = 8 cm) was used to loosely focus the horizontally polarized fundamental beam into the designed hologram sample (S) with a spot size slightly larger than the diameter of the hologram, so that the hologram with a diameter of 152 μm can be homogeneously covered by the pump laser. In this configuration of an ordinary (o)-polarized pump laser, only the oo–e interaction is available to reconstruct the nonlinear holographic image *via* the nonlinear coefficient of d_{31} in the sample. A short-band-pass filter (F) was used to filter out the fundamental beam, and then the emitted SH signal was collected by lens L2 (focal length f = 5 cm) and then recorded using a CMOS camera (Prime 95B, PHITIMETRICS) and a spectrometer (Acton 2500i with Pixis CCD camera, Princeton Instruments). The collection Lens L2 was mounted on a *z*-translation stage, which enabled the SHG intensity measurements either in the far field or the near field. Furthermore, to measure the SHG in the near field, we introduced a confocal microscope system by adding a 10 cm focal lens L3 before the CMOS camera and spectrometer, respectively. Then the SHG in the near field could be obtained by properly setting the distance between L2 and the sample.

Conflicts of interest

The authors declare no competing financial interests.

Acknowledgements

This work was supported by the National Natural Science Foundation of China (No. 91850113, 11774115 and 11904271), the 973 Programs under grants 2014CB921301, the Postdoctoral Science and Technology Activities Preferred Financing Project in Hubei Province, the Basic and Applied Basic Research Major Program of Guangdong Province (No.

2019B030302003) and the Qatar National Research Fund (grant # NPRP12S-0205-190047).

References

1 V. Berger, *Phys. Rev. Lett.*, 1998, **81**, 4136–4139.
2 N. G. R. Broderick, G. W. Ross, H. L. Offerhaus, D. J. Richardson and D. C. Hanna, *Phys. Rev. Lett.*, 2000, **84**, 4345–4348.
3 A. Arie and N. Voloch, *Laser Photonics Rev.*, 2010, **4**, 355–373.
4 T. Xu, K. Switkowski, X. Chen, S. Liu, K. Koynov, H. Yu, H. Zhang, J. Wang, Y. Sheng and W. Krolikowski, *Nat. Photonics*, 2018, **12**, 591–595.
5 D. Wei, C. Wang, H. Wang, X. Hu, D. Wei, X. Fang, Y. Zhang, D. Wu, Y. Hu, J. Li, S. Zhu and M. Xiao, *Nat. Photonics*, 2018, **12**, 596–600.
6 J. A. Armstrong, N. Bloembergen, J. Ducuing and P. S. Pershan, *Phys. Rev.*, 1962, **127**, 1918–1939.
7 M. M. Fejer, D. H. Jundt, R. L. Byer and G. A. Magel, *IEEE J. Quantum Electron.*, 1992, **28**, 2631–2654.
8 Y. Q. Qin, C. Zhang, Y. Y. Zhu, X. P. Hu and G. Zhao, *Phys. Rev. Lett.*, 2008, **100**, 063902.
9 N. V. Bloch, K. Shemer, A. Shapira, R. Shiloh, I. Juwiler and A. Arie, *Phys. Rev. Lett.*, 2012, **108**, 233902.
10 D. Liu, S. Liu, L. M. Mazur, B. Wang, P. Lu, W. Krolikowski and Y. Sheng, *Appl. Phys. Lett.*, 2020, **116**, 051104.
11 R. V. Roussev, C. Langrock, J. R. Kurz and M. M. Fejer, *Opt. Lett.*, 2004, **29**, 1518–1520.
12 D. Mazzotti, P. De Natale, G. Giusfredi, C. Fort, J. A. Mitchell and L. W. Hollberg, *Appl. Phys. B*, 2000, **70**, 747–750.
13 H. G. D. Chatellus, A. V. Sergienko, B. E. A. Saleh, M. C. Teich and G. D. Giuseppe, *Opt. Express*, 2006, **14**, 10060–10072.
14 Y. Sheng, K. Koynov, J. Dou, B. Ma, J. Li and D. Zhang, *Appl. Phys. Lett.*, 2008, **92**, 201113.
15 Y. Niu, C. Lin, X. Liu, Y. Chen, X. Hu, Y. Zhang, X. Cai, Y. X. Gong, Z. Xie and S. Zhu, *Appl. Phys. Lett.*, 2020, **116**, 101104.
16 C. Wang, C. Langrock, A. Marandi, M. Jankowski, M. Zhang, B. Desiatov, M. M. Fejer and M. Lončar, *Optica*, 2018, **5**, 1438–1441.
17 X. W. Luo, Q. Y. Zhang, P. Xu, R. Zhang, H. Y. Liu, C. W. Sun, Y. X. Gong, Z. D. Xie and S. N. Zhu, *Phys. Rev. A*, 2019, **99**, 063833.
18 L. L. Lu, P. Xu, M. L. Zhong, Y. F. Bai and S. N. Zhu, *Opt. Express*, 2015, **23**, 1203–1212.
19 J. Lu, J. B. Surya, X. Liu, A. W. Bruch, Z. Gong, Y. Xu and H. X. Tang, *Optica*, 2019, **6**, 1455–1460.
20 R. Wolf, Y. Jia, S. Bonaus, S. W. Christoph, S. J. Herr, I. Breunig, K. Buse and H. Zappe, *Optica*, 2018, **5**, 872–875.
21 L. Chang, Y. Li, N. Volet, L. Wang, J. Peters and J. E. Bowers, *Optica*, 2016, **3**, 531–535.
22 J. R. Kurz, A. M. Schober, D. S. Hum, A. J. Saltzman and M. M. Fejer, *IEEE J. Sel. Top. Quantum Electron.*, 2002, **8**, 660–664.
23 T. Ellenbogen, N. Voloch-Bloch, A. Ganany-Padowicz and A. Arie, *Nat. Photonics*, 2009, **3**, 395–398.
24 S. Liu, K. Switkowski, C. Xu, J. Tian, B. Wang, P. Lu, W. Krolikowski and Y. Sheng, *Nat. Commun.*, 2019, **10**, 3208.
25 D. Wei, C. Wang, X. Xu, H. Wang, Y. Hu, P. Chen, J. Li, Y. Zhu, C. Xin, X. Hu, Y. Zhang, D. Wu, J. Chu, S. Zhu and M. Xiao, *Nat. Commun.*, 2019, **10**, 4193.
26 S. Chen, G. Li, K. W. Cheah, T. Zentgraf and S. Zhang, *Nanophotonics*, 2018, **7**, 1013–1024.
27 G. Li, S. Zhang and T. Zentgraf, *Nat. Rev. Mater.*, 2017, **2**, 17010.
28 G. Hu, X. Hong, K. Wang, J. Wu, H.-X. Xu, W. Zhao, W. Liu, S. Zhang, F. Garcia-Vidal, B. Wang, P. Lu and C.-W. Qiu, *Nat. Photonics*, 2019, **13**, 467–472.
29 X. Hong, G. Hu, W. Zhao, K. Wang, S. Sun, R. Zhu, J. Wu, W. Liu, K. P. Loh, A. T. S. Wee, B. Wang, A. Alù, C. W. Qiu and P. Lu, *Research*, 2020, **2020**, 1–10.
30 M. Yamada, N. Nada, M. Saitoh and K. Watanabe, *Appl. Phys. Lett.*, 1993, **62**, 435–436.
31 X. Chen, P. Karpinski, V. Shvedov, K. Koynov, B. Wang, J. Trull, C. Cojocaru, W. Krolikowski and Y. Sheng, *Appl. Phys. Lett.*, 2015, **107**, 141102.
32 S. Matsumoto, E. J. Lim, H. M. Hertz and M. M. Fejer, *Electron. Lett.*, 1991, **27**, 2040–2042.
33 V. Y. Shur, V. A. Shikhova, D. O. Alikin, V. A. Lebedev, L. I. Ivleva, J. Dec, D. C. Lupascu and V. V. Shvartsman, *Sci. Rep.*, 2017, **7**, 125.
34 A. Shapira, R. Shiloh, I. Juwiler and A. Arie, *Opt. Lett.*, 2012, **37**, 2136–2138.
35 X. H. Hong, B. Yang, C. Zhang, Y. Q. Qin and Y. Y. Zhu, *Phys. Rev. Lett.*, 2014, **113**, 163902.
36 A. Shapira, I. Juwiler and A. Arie, *Laser Photonics Rev.*, 2013, **7**, L25–L29.
37 K. Shemer, N. Voloch-Bloch, A. Shapira, A. Libster, I. Juwiler and A. Arie, *Opt. Lett.*, 2013, **38**, 5470–5473.
38 V. Pasiskevicius, *Nat. Photonics*, 2009, **3**, 374–375.
39 S. Trajtenberg-Mills, I. Juwiler and A. Arie, *Optica*, 2017, **4**, 153–156.
40 B. Yang, X. H. Hong, R. E. Lu, Y. Y. Yue, C. Zhang, Y. Q. Qin and Y. Y. Zhu, *Opt. Lett.*, 2016, **41**, 2927–2929.
41 B. R. Brown and A. W. Lohmann, *Appl. Opt.*, 1966, **5**, 967–969.
42 A. W. Lohmann and D. P. Paris, *Appl. Opt.*, 1967, **6**, 1739–1748.
43 R. W. Gerchberg and W. O. Saxton, *Optik*, 1972, **35**, 1–6.
44 Y. Sheng, A. Best, H. J. Butt, W. Krolikowski, A. Arie and K. Koynov, *Opt. Express*, 2010, **18**, 16539–16545.
45 M. Scalora and M. E. Crenshaw, *Opt. Commun.*, 1994, **108**, 191–196.
46 S. M. Saltiel, D. N. Neshev, W. Krolikowski, A. Arie, O. Bang and Y. S. Kivshar, *Opt. Lett.*, 2009, **34**, 848–850.

47 C. David, A. Tunyagi, K. Betzler and M. Wöhlecke, *Phys. Status Solidi B*, 2007, **244**, 2127–2137.
48 D. C. Burnham and D. L. Weinberg, *Phys. Rev. Lett.*, 1970, **25**, 84–87.
49 Y. Zhang, J. Wen, S. N. Zhu and M. Xiao, *Phys. Rev. Lett.*, 2010, **104**, 183901.
50 P. Molina, M. D. Ramírez and L. E. Bausá, *Adv. Funct. Mater.*, 2008, **18**, 709–715.
51 J. Trull, C. Cojocaru, R. Fischer, S. M. Saltiel, K. Staliunas, R. Herrero, R. Vilaseca, D. N. Neshev, W. Krolikowski and Y. S. Kivshar, *Opt. Express*, 2007, **15**, 15868–15877.